RSC Advances

PAPER

View Article Online
View Journal | View Issue

Cite this: *RSC Adv.*, 2025, **15**, 19515

Fabrication and properties of PANI-ZnO/SiO_2 photothermal corrosion-resistant integrated coating on aluminum alloy surfaces

Zhaowei Liu,[a] Zechong Liu,[a] Tao Wu,[a] Pengjiao Chong,[ab] Chen Tang[ab] and Yufei Tang *[a]

Icing severely damages outdoor equipment, such as power transmission lines and wind turbine blades, posing safety hazards. Utilizing photothermal materials to construct anti-icing coatings is a promising approach. However, existing photothermal hydrophobic coatings suffer from low light absorption efficiency and slow heating rates, limiting their widespread application. Therefore, developing coatings that integrate simple and efficient de-icing and corrosion-resistant functions is urgent. In this study, ZnO-coated SiO_2 particles were synthesized *via in situ* chemical reactions, and a PANI-ZnO/SiO_2 photothermal corrosion-resistant integrated composite coating was constructed on the surface of aluminum alloy. Results showed that the obtained PZS-1.0 coating had a three-dimensional coral-like network structure. Under sunlight, the photothermal composite coating achieved a temperature rise (ΔT) of 74 °C within 90 seconds. Notably, due to the synergistic photothermal effect of ZnO and PANI, the bottom of a completely frozen droplet was initiated to melt within 20 seconds and fully melted within 80 seconds, with the surface temperature reaching 17.8 °C. Importantly, excellent corrosion resistance was demonstrated by the coating, with a self-corrosion potential (E_{corr}) of −681.07 mV and a maximum polarization resistance of 4307 Ω cm^2. This photothermal corrosion-resistant integrated coating offers a new solution for the application of aluminum alloy in high-voltage transmission and marine engineering, showing broad application prospects.

Received 27th April 2025
Accepted 20th May 2025

DOI: 10.1039/d5ra02954f

rsc.li/rsc-advances

Introduction

Icing in extreme cold weather poses a severe threat to the normal operation of wind turbine blades and power transmission lines.[1,2] Traditional active de-icing techniques, such as chemical de-icing or electric heating, often suffer from high energy consumption, complex operation, and environmental unfriendliness.[3,4] In recent years, superhydrophobic coatings that reduce water droplet adhesion by lowering surface energy or improving micro/nanostructures have attracted significant research attention.[5,6] However, icing remains inevitable under prolonged low-temperature conditions. Studies have shown that integrating these coatings with photothermal materials to create photothermal superhydrophobic coatings not only reduces water droplet adhesion and icing but also leverages the unique advantage of converting solar energy into heat to melt interfacial ice layers, achieving efficient de-icing.[7–9] This composite coating technology does not rely on active de-icing methods and has broad application prospects due to its green, energy-saving, and sustainable properties, providing sustainable and innovative solutions to address the challenges of extreme weather conditions. Xie *et al.*[10] fabricated a photothermal anti-icing material consisting of a substrate, a carbon-based light-absorption layer, and an encapsulation layer using a combination template spraying method. The average surface temperature of the material could reach 85 °C after exposure to sunlight, and the frost or ice layer would melt and peel off from the surface after 300 seconds of exposure. Cheng *et al.*[11] prepared a multifunctional magnetic hybrid coating with excellent superhydrophobicity, wetting stability, long ice-delaying performance, and superior thermal de-icing properties by mixing MNPs as a heat medium with amino-modified Fe_3O_4 particles and then cross-linking with diethylenetriamine. However, existing photothermal materials still face issues such as low light absorption efficiency, slow heating rates, and poor cyclic durability. How to achieve efficient anti-icing and de-icing effects through interfacial optimization in multi-component materials remains one of the key challenges to overcome. Moreover, the current anti-corrosion mechanism based on multi-component synergy still requires further explanation.

Therefore, in this study, ZnO-coated SiO_2 particles were synthesized *via in situ* chemical reactions, and a photothermal

[a]*Department of Materials Science and Engineering & Shaanxi Province Key Laboratory of Corrosion and Protection, Xi'an University of Technology, Xi'an 710048, P. R. China. E-mail: yftang@xaut.edu.cn*

[b]*Wenzhou Anneng Technology Co., Ltd, Wenzhou 325000, P. R. China*

corrosion-resistant integrated poly(aniline)-based composite coating was constructed on the surface of aluminum alloy using *in situ* polymerization. The microstructure, composition, and photothermal properties of the composite coatings under different ratios were investigated. The regulatory effects of the ratios on the coating properties were elucidated through studies on photothermal de-icing and corrosion-resistant performances. Moreover, this study provided an interpretation of the corrosion protection mechanism beyond conventional surface barrier effects. It revealed the synergistic contributions of the physical barrier, PANI-induced cathodic protection, and passivation layer formation *via* interfacial enrichment. This integrated mechanism offered a understanding of multi-component corrosion resistance compared to previous single-mechanism models.

Experimental procedure

Materials and methods

Solution A was prepared by mixing 0.528 g of zinc acetate with 60 mL of ethanol, and Solution B was prepared by mixing 0.162 g of NaOH with 60 mL of ethanol. SiO_2 particles were sequentially immersed in Solutions A and B for 5 min each, followed by drying at 125 °C. This process was repeated three times to obtain ZnO/SiO_2 particles. The ZnO/SiO_2 particles were dispersed in 25 mL of ethanol, and then 8 mL of hydrochloric acid, 0.5 g of aniline, and 2 mL of KH-550 were added sequentially. Ammonium persulfate was added according to the mass ratios of Ani/APS of 0.5, 1.0, 1.5, and 2.0, and the mixture was continuously stirred for 6 h in an ice bath to obtain the PANI-ZnO/SiO_2 composite. Then the composite was ultrasonically dispersed in *n*-hexane with PDMS (mass ratio of 1 : 1), followed by the addition of 0.05 g of curing agent and stirring for 10 minutes. The mixture was sprayed onto an aluminum substrate and dried at 80 °C for 2 h to obtain the photothermal corrosion-resistant integrated composite coating. The PANI-ZnO/SiO_2 composites obtained with different Ani/APS ratios were named PZS-x, where $x = 0.5$, 1.0, 1.5, or 2.0, respectively.

Characterization

The microstructure and roughness of the composite coating were characterized by scanning electron microscopy and atomic force microscopy. The photothermal response of the composite coating was recorded using a FLIR ONE PRO (IOS) thermal imager under simulated sunlight provided by a CEL-HXF300-T3 xenon lamp source system in a dark environment. The photothermal conversion efficiency (η) was subsequently investigated, and its calculation was based on the following equation:

$$\mathrm{hS} = \frac{mC_\mathrm{P}}{\tau} \quad (1)$$

$$\eta = \frac{\mathrm{hS} \times (T_\mathrm{max} - T_0)}{I \times s \times \left(1 - 10^{-A_\lambda}\right)} \quad (2)$$

In the equation, hS denoted the heat transfer coefficient; m referred to the total mass of the sample; C_p was the average specific heat capacity of the sample, which was 0.87 J g^{-1} K^{-1}; τ represented the cooling time constant; T_max represented the maximum steady-state temperature during the heating process; T_0 referred to the initial ambient temperature; I represented the incident light intensity; s indicated the illuminated surface area; and A_λ was the absorbance of the material at the excitation wavelength, which was 0.90.

The photothermal de-icing performance of the composite coating was tested in a constant temperature and humidity chamber, with the temperature set at 20 °C and a 20 μL droplet added to the sample surface after pre-cooling for 1 h. The corrosion resistance of the samples was measured using an electrochemical workstation (CS310 H, Corrtest). The counter electrode, reference electrode, and working electrode were platinum mesh (10 mm × 10 mm), SCE electrode, and the PZS-coated aluminum alloy sample, respectively.

Results and discussion

Microstructure and composition of PZS coating

Fig. 1 presented the FT-IR spectra of the PZS samples. As shown in the figure, all PZS samples exhibited similar peak positions. A characteristic N–H stretching vibration of amine groups and –OH absorption appeared at 3655 cm^{-1}; the C=C stretching vibration of the benzene ring was observed at 1507 cm^{-1}; the in-plane C–H stretching vibration of protonated PANI appeared at 1134 cm^{-1}; the asymmetric and symmetric stretching vibrations of Si–O–Si were detected at 1070 cm^{-1} and 802 cm^{-1}, respectively; and the stretching vibration of the Zn–O bond was found at 450 cm^{-1}. The presence of these characteristic peaks indicated the successful formation of the PANI–ZnO/SiO_2 structure in all PZS samples.

Fig. 2 was the SEM images of the composite coatings obtained with varying Ani : APS ratios. It could be seen that the PZS-0.5 coating consisted of blocky aggregates formed by the agglomeration of numerous particles. As the Ani : APS ratio increased, the coating surface transitioned from a blocky structure to a coral-like network structure. Upon further increasing the ratio, the continuity of the coral-like structure in the PZS-1.5 and PZS-2.0 coatings was significantly reduced. This was attributed to the effect of the Ani : APS ratio on the amount of PANI. During the synthesis process, the amount of PANI produced gradually decreased with the increase of the Ani : APS

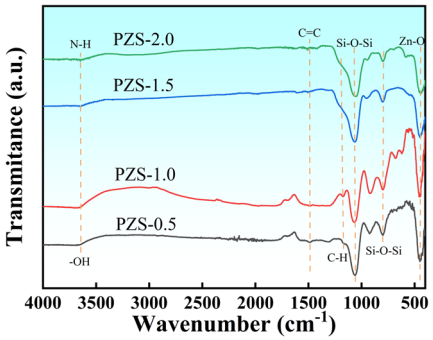

Fig. 1 The FT-IR spectra of the PZS samples.

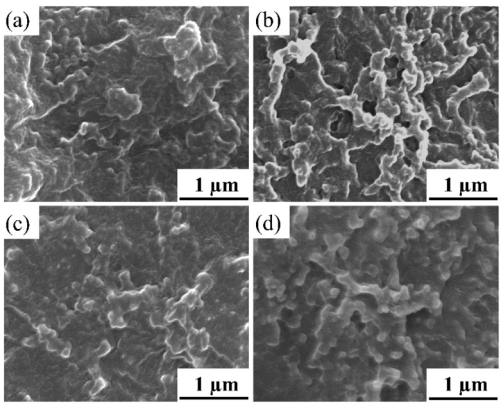

Fig. 2 SEM images of the composite coatings obtained with varying Ani : APS ratios (a) PZS-0.5, (b) PZS-1.0, (c) PZS-1.5, (d) PZS-2.0.

ratio. Since PANI acted as a connecting phase between ZnO/SiO_2 particles, the reduction of its content weakened the bridging effect between particles, leading to the transition from a blocky structure to a three-dimensional coral-like network structure. This structural change was likely to affect the absorption and reflection of light, thereby altering the photothermal conversion performance.

Fig. 3 showed the cross-sectional SEM images of the various PZS composite coatings. The coating thicknesses, from highest to lowest, were PZS-1.0 (35.0 μm), PZS-0.5 (32.5 μm), PZS-1.5 (27.5 μm), and PZS-2.0 (17.5 μm). Among them, the PZS-1.0 coating clearly exhibited the highest pore density, which was beneficial to photothermal conversion. Therefore, PZS-1.0 was considered to exhibit the best photothermal performance, which was consistent with the analysis results in Fig. 2.

Fig. 4 showed the surface roughness and elemental distribution of the PZS-1.0 coating. As seen in Fig. 4(a), the coating's surface roughness (R_a) value was approximately 23.14 nm. Studies had shown that an R_a value close to 20 nm could effectively trigger Rayleigh scattering of the coating in the near-infrared region.[12] This induced random deflection of near-infrared light waves during propagation, lengthening the path and enhancing broadband absorption efficiency. The elemental distribution maps revealed that Si, N, and Zn were evenly distributed across the coating, indicating no severe agglomeration of ZnO/SiO_2 particles in the PZS-1.0 coating. Importantly, this nanoscale roughness and uniform distribution exposed more active sites of ZnO, which was expected to promote the separation and transport of photogenerated carriers, thereby enhancing the coating's photothermal conversion performance.

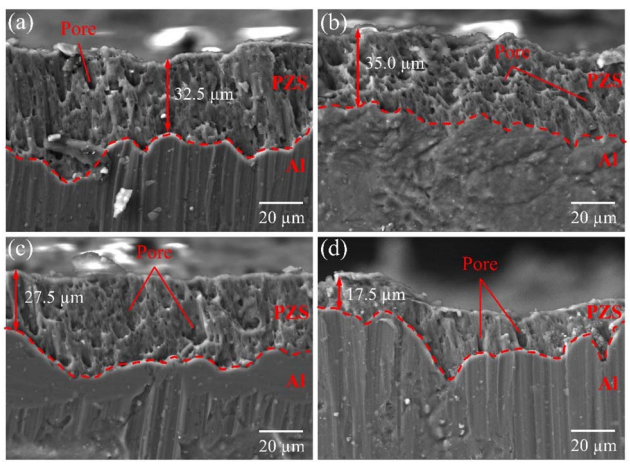

Fig. 3 Cross-sectional SEM images of different PZS composite coatings: (a) PZS-0.5, (b) PZS-1.0, (c) PZS-1.5, (d) PZS-2.0.

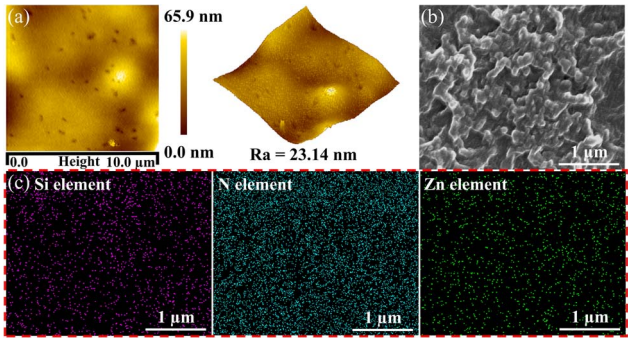

Fig. 4 Surface roughness and composition of the PZS-1.0 coating (a) surface roughness, (b) SEM and (c) the elemental distribution of N, Si and Zn.

Photothermal performance of PZS coating

To elucidate the relationship between the microstructure of the coatings and their photothermal performance, quantitative characterization was conducted through photothermal conversion experiments, with the results presented in Fig. 5. Fig. 5(a)

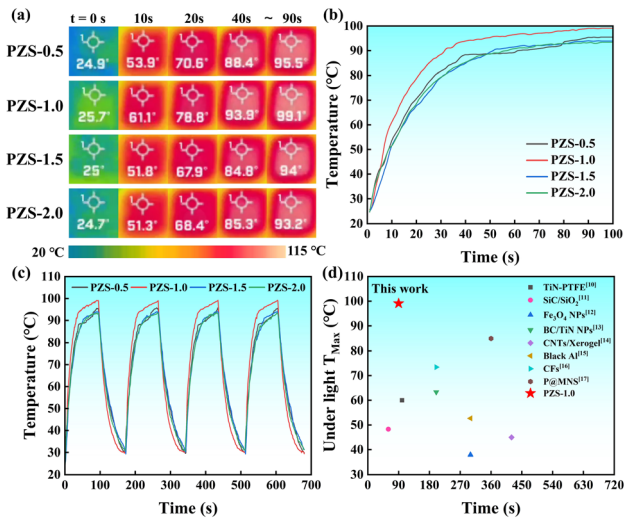

Fig. 5 Photothermal performance of PZS coating (a) thermographic images of the photothermal conversion, (b) temperature–time curves, (c) stability results, (d) performance comparison with other photothermal coatings reported in previous literature (TiN-PTFE,[13] SiC/SiO_2,[14] Fe_3O_4 NPs,[11] BC/TiN NPs,[8] CNTs/Xerogel,[15] black Al,[16] CFs,[17] P@MNS[10]).

showed the thermographic images of the photothermal conversion for the PZS coatings. It was found that the surface temperature of all coatings increased above 90 °C within 90 seconds, demonstrating excellent photothermal conversion performance, which was attributed to the synergistic photothermal effect dominated by PANI and assisted by ZnO. Notably, the PZS-1.0 sample exhibited the strongest photothermal response. At 90 seconds, its surface temperature reached 99.1 °C ($\eta = 95.3\%$), which was significantly higher than that of the PZS-0.5 coating at the same time point. This may be due to the three-dimensional coral-like network structure of the PZS-1.0 coating, which not only ensured the light absorption capabilities of ZnO and PANI but also extended the light propagation path, thereby enhancing the photothermal conversion efficiency. However, as the amount of PANI gradually decreased, the surface temperatures of the PZS-1.5 and PZS-2.0 coatings dropped sharply. This was because PANI itself has light absorption capabilities, and reducing its content affected the photothermal conversion efficiency. Combining the temperature–time curves (Fig. 5(b)) and stability test results (Fig. 5(c)), it was clearly observed that the PZS-1.0 coating maintained a high temperature throughout the entire period. Furthermore, as shown in Fig. 5(c), during multiple heating/cooling cycles, the heating and cooling rates remained nearly constant under continuous light irradiation and natural cooling conditions, exhibiting a highly consistent trend. The high reproducibility of these thermal response curves indicated that the photothermal response capability of the coating did not degrade significantly throughout repeated thermal cycling, demonstrating excellent photothermal conversion stability. In addition, the consistent thermal behavior reduced the risk of thermal fatigue, which contributed to maintaining long-term operational stability under complex environmental conditions, thereby ensuring the safety and reliability of the coating in photothermal anti-icing applications. A comparison with other photothermal coatings reported in previous literature[8,10,11,13–17] is shown in Fig. 5(d). In this study, the PZS-1.0 coating achieved a temperature rise (ΔT) of 74 °C within 90 seconds under short-time irradiation. Compared to other photothermal coatings such as TiN PTFE[13] and SiC/SiO_2,[14] the temperature rise within the same time period is greater, demonstrating excellent performance advantages and enormous potential for photothermal de icing applications.

To verify the freezing/thawing behavior of the photothermal coatings, tests were conducted, with the results shown in Fig. 6. At the temperature of −20 °C, water droplets on the surface of the PZS-1.0 coating completely froze within 240 seconds. Subsequently, the xenon lamp was turned on to simulate sunlight, and it was observed that the bottom of the ice droplet began to melt after 20 seconds, with the surface temperature reaching 2.1 °C. After continuous irradiation for 80 seconds, the ice droplet on the coating surface completely melted, and the surface temperature reached 17.8 °C. Comparing the surface temperature changes of different photothermal coatings, it was found that the temperature change curves of the PZS coating samples were highly similar. The differences in their photothermal de-icing performance mainly depended on the slow temperature increase in the 3–5 °C range, corresponding to the latent heat absorption stage of the ice droplet. Among them, the PZS-1.0 coating had the shortest de-icing response time, with its surface temperature beginning to rise rapidly after only 40 seconds. The de-icing response times of the other photothermal coatings gradually increased but all began to rise sharply within 50 seconds. This indicates that the prepared PZS composite coatings possess good photothermal de-icing performance.

Corrosion resistance of PZS coating

In practical applications, the photothermal coatings on aluminum alloy substrates also need to exhibit good corrosion resistance. Therefore, the corrosion behavior of the PZS coatings was investigated using an electrochemical workstation, with the results shown in Fig. 7. By comparing the self-corrosion potential (E_{corr}) and self-corrosion current density (I_{corr}) values of the samples, their corrosion resistance could be evaluated. A more positive E_{corr} value indicates better corrosion resistance and a lower tendency for corrosion, while a smaller I_{corr} value suggests a lower corrosion rate. Combining the polarization curves (Fig. 7(a)) and the self-corrosion test results (Table 1), it

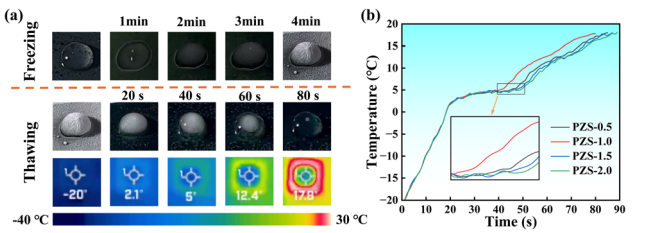

Fig. 6 Freezing/thawing behavior of water droplet on PZS coating (a) thermographic images, (b) temperature–time curves (The inset is magnified view).

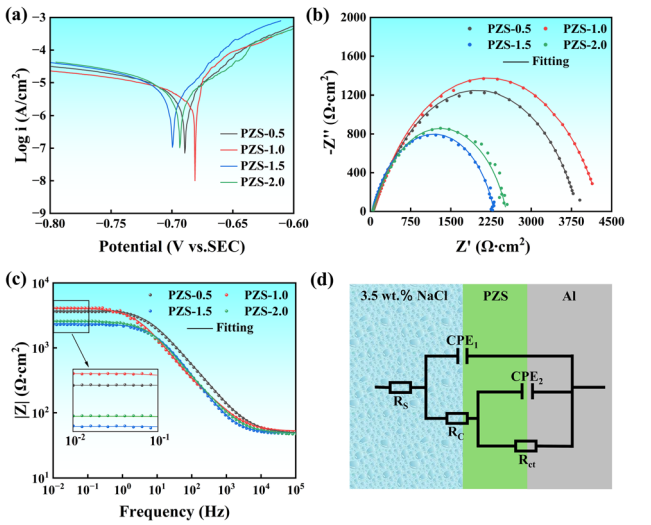

Fig. 7 Corrosion behavior of the PZS coating (a) dynamic potential polarization curve, (b) Nyquist plot, (c) Bode (F-|Z|) plot (The inset is magnified view), (d) equivalent circuit model.

Table 1 Self-corrosion test results of PZS coating in 3.5 wt% NaCl solution

Sample	E_{corr} (mV_{SCE})	I_{corr} ($\mu A\ cm^{-2}$)
PZS-0.5	−689.46 ± 0.2	6.999 ± 0.3
PZS-1.0	−681.07 ± 0.2	6.274 ± 0.1
PZS-1.5	−699.62 ± 0.1	7.214 ± 0.1
PZS-2.0	−693.85 ± 0.3	7.466 ± 0.2

was observed that the PZS-1.0 sample had the most positive E_{corr} value (−681.07 mV) and the smallest I_{corr} value (6.27×10^{-6} A cm^{-2}). As the amount of PANI in the coating decreased, the E_{corr} values of the samples gradually shifted to more negative values, and the I_{corr} values increased. Therefore, the PZS-1.0 sample exhibited the lowest corrosion rate and the best corrosion resistance.

Further evaluation of the corrosion resistance of the photothermal coatings was conducted using electrochemical impedance spectroscopy (EIS). From the Nyquist plot (Fig. 7(b)), it was observed that the PZS-1.0 sample exhibited the largest semicircle radius, indicating a higher resistance and thus stronger corrosion resistance. The Bode plot (Fig. 7(c)) revealed differences in the impedance modulus values of the PZS samples in the low-frequency range (0.01–1 Hz), which represent the polarization resistance (R_p), the sum of the coating resistance and charge transfer resistance. Among them, the PZS-1.5 sample had the lowest polarization resistance value at 0.01 Hz, only 2.27×10^3 Ω cm^2 ($|Z|_{0.01Hz}$), while the PZS-1.0 sample had the highest value, reaching 4.30×10^3 Ω cm^2 ($|Z|_{0.01Hz}$). The higher the polarization resistance value, the stronger the corrosion resistance, confirming that the PZS-1.0 sample had the best corrosion resistance, consistent with the analysis from the Nyquist plot. The equivalent circuit model for the corrosion process of the coating was constructed using Zsimpwin software, and the experimental data from Fig. 7(b) and (c) were fitted. The equivalent circuit was shown in Fig. 7(d), and the fitting parameters were listed in Table 2. In the equivalent circuit, R_s represents the solution resistance, reflecting the impedance between the solution and the electrode; R_c is the coating resistance; and R_{ct} is the charge transfer resistance. Considering the porous structure of the coating and the roughness of the electrode surface, a constant phase element (CPE) was used instead of an ideal capacitor. CPE_1 represents the capacitance of the coating, in parallel with R_c, and CPE_2 represents the double-layer capacitance between the solution and the metal substrate, in parallel with R_{ct}. In a 3.5 wt% NaCl solution at 25 °C, the solution resistance R_s was approximately 48.1 ± 2 Ω cm^2. As the amount of PANI decreased, the coating resistance R_c increased from 568 Ω cm^2 for PZS-0.5 to 1944 Ω cm^2 for PZS-2.0. The charge transfer resistance R_{ct}, which reflects the coating's resistance to localized corrosion or pitting, was highest for the PZS-1.0 sample at 3171 Ω cm^2, indicating the strongest pitting resistance. Generally, a higher polarization resistance ($R_p = R_c + R_{ct}$) indicates stronger corrosion resistance. The PZS-1.0 sample exhibited the highest R_p value of 4307 Ω cm^2, with the charge transfer resistance R_{ct} accounting for 73.6% of the total. This result indicated that the interfacial charge transfer process was significantly hindered which reduced the corrosion reaction rate and enhanced the protective performance of the coating.

The protective effect of PANI arises from its redox buffering ability and electronic conductivity. During corrosion, PANI undergoes redox transitions between its emeraldine and pernigraniline states, which facilitated electron transfer and promoted the cathodic reduction of dissolved oxygen. Furthermore, the formation of a passivating oxide layer was enhanced by the generation of OH^- at cathodic sites, which reacted with Al^{3+} ions to form $Al(OH)_3$ and subsequently Al_2O_3. These processes jointly contributed to the increased charge transfer resistance (R_{ct}) and overall impedance observed in the EIS spectra.

Fig. 8 was the photothermal corrosion-resistant mechanism of the PZS coating. When sunlight irradiated the PZS coating, the semiconductor ZnO particles embedded within completed energy conversion through photon absorption, carrier excitation, and non-radiative recombination vibrational heating.[18] However, this process was typically concentrated in the ultraviolet region. The effective synthesis of PANI enabled it to leverage its broad-spectrum absorption characteristics based on the conjugated π structure and the polaron energy relaxation

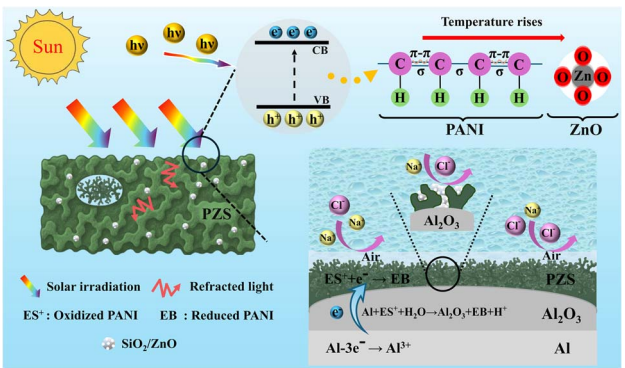

Fig. 8 Photothermal corrosion-resistant mechanism of the PZS coating.

Table 2 Equivalent circuit fitting parameters

Sample	R_s (Ω cm^2)	Q_{CPE_1} ($\Omega^{-1}\ cm^{-2}\ s^n$)	n_1	R_c (Ω cm^2)	Q_{CPE_2} ($\Omega^{-1}\ cm^{-2}\ s^n$)	n_2	R_{ct} (Ω cm^2)
PZS-0.5	46.80	2.02×10^{-5}	0.74	568	9.34×10^{-7}	0.84	2982
PZS-1.0	49.84	1.65×10^{-5}	0.76	1136	8.17×10^{-8}	0.94	3171
PZS-1.5	47.15	1.47×10^{-5}	0.80	1304	1.82×10^{-5}	0.72	959
PZS-2.0	48.82	1.49×10^{-5}	0.73	1634	3.225×10^{-6}	0.95	1256

mechanism after HCl doping, resulting in strong absorption in the visible-near-infrared region.[19] This effectively compensated for the spectral limitation of ZnO's sole UV absorption. After combination, the light capture efficiency was significantly enhanced, demonstrating excellent photothermal properties. On the other hand, the rough structure of the hydrophobic coating surface could form an air cushion with NaCl solution, thereby isolating the intrusion of corrosive media.[20] The SiO_2/ZnO particles further enhanced the surface roughness, facilitating the formation of the air cushion. Importantly, the HCl-doped polyaniline as an oxidized conductive emeraldine salt (ES), underwent redox transformation during the corrosion process and simultaneously promoted the reduction of dissolved oxygen during its oxidation. This redox activity contributed to the anodic passivation of the aluminum alloy surface. As a result, Al^{3+} ions released from the substrate reacted with OH^- in water to form $Al(OH)_3$, which subsequently dehydrated to form a dense and stable Al_2O_3 protective layer. Therefore, polyaniline functioned as an active corrosion-inhibiting layer during the corrosion process. Additionally, due to its coral-like structure, PANI also served to some extent as a physical barrier. However, when the amount of PANI was significantly reduced, it became difficult to fully cover the substrate. The doped protons (H^+) might undergo exchange or neutralization reactions with Cl^- ions in the NaCl solution, resulting in decreased conductivity of PANI and loss of its electrochemical protective function.[21] Therefore, the amount of PANI in the coating directly affected the photothermal performance and corrosion resistance of the aluminum alloy substrate.

Conclusions

In this study, aiming to address the issues of low light absorption efficiency and slow heating rates in photothermal hydrophobic coatings, a solution was proposed involving the *in situ* chemical synthesis of ZnO-coated SiO_2 particles and the construction of a PANI-ZnO/SiO_2 photothermal corrosion-resistant integrated composite coating on the surface of aluminum alloy. The results indicated that the surface of the prepared PZS-1.0 composite coating featured a three-dimensional coral-like network structure with a surface roughness (R_a) value of 23.14 nm. This structure could extend the light propagation path through Rayleigh scattering, thereby enhancing light capture efficiency. Benefiting from the synergistic photothermal effect of ZnO and PANI, the temperature rise (ΔT) of the PZS-1.0 coating reached 74 °C within 90 seconds under short-time irradiation. Moreover, it enabled the bottom of a completely frozen droplet to begin melting within 20 seconds, with complete melting achieved within 80 seconds. It was worth noting that this study discussed in detail the corrosion resistance mechanism of the PZS coating. The results indicated that the coating exhibited a self-corrosion potential (E_{corr}) of −681.07 mV and a maximum polarization resistance of 4307 Ω cm^2, demonstrating excellent corrosion performance. This suggests that the developed photothermal corrosion-resistant integrated coating holds promise for applications in high-voltage transmission, marine engineering, and other fields, showcasing broad application potential. In the future, we will conduct in-depth investigations into the durability of the coating and the mechanisms of performance degradation under complex working conditions.

Data availability

The authors declare that the data supporting the findings of this study are available within the article.

Author contributions

Zhaowei Liu: formal analysis, methodology, writing – original draft. Zechong Liu: validation, investigation, data curation. Tao Wu: data curation, visualization. Pengjiao Chong: validation, investigation. Chen Tang: data curation. Yufei Tang: conceptualization, resources, supervision, funding acquisition.

Conflicts of interest

The authors declare that there are no competing financial interests.

Acknowledgements

The authors gratefully acknowledge the support from the National Natural Science Foundation of China (No. 52172074), Shaanxi Province Natural Science Basic Research Program (2024JC-YBQN-0565).

References

1 R. Veerakumar, L. Gao, Y. Liu and H. Hu, *Cold Reg. Sci. Technol.*, 2015, **169**, 102908.
2 N. N. Nguyen, S. Davani, R. Asmatulu, M. Kapple, R. Berger and H. J. Butt, *ACS Appl. Nano Mater.*, 2022, **5**(12), 19017–19024.
3 Y. Liu, R. Xu, N. Luo, Y. Liu, Y. Wu, B. Yu, S. Liu and F. Zhou, *Adv. Mater. Technol.*, 2021, **6**(11), 2100371.
4 Y. Zhang, X. Fan, X. Li, Z. Zhang, Y. Zhang, Z. Chen, S. Ge, Y. Wang and M. Zhu, *Chem. Eng. J.*, 2024, **498**, 155101.
5 T. Muangnapoh, N. Janampansang, S. Chuphong, C. Chevachotivut, B. Traipattanakul, P. Kumnorkaew and T. Sodsai, *Colloid Interface Sci. Commun.*, 2023, **57**, 100745.
6 M. Wu, Y. Liu, Z. Zhang, Y. Wang, H. He, H. Zhu, K. Xu, J. Wang and J. Lu, *Surf. Coat. Technol.*, 2024, **483**, 130820.
7 F. Chu, Z. Hu, Y. Feng, N. C. Lai, X. Wu and R. Wang, *Adv. Mater.*, 2024, **36**(31), 2402897.
8 B. Wang, P. Yu, Q. Yang, Z. Jing, W. Wang, P. Li, X. Tong, F. Lin, D. Wang, G. E. Lio, R. Caputo, O. Ávalos-Ovando, A. O. Govorov, H. Xu and Z. M. Wang, *Mater. Today Phys.*, 2022, **24**, 100683.
9 Y. Xue, P. Verdross, W. Liang, R. T. Woodward and A. Bismarck, *Adv. Colloid Interface Sci.*, 2025, **341**, 103489.
10 Z. Xie, H. Wang, M. Li, Y. Tian, Q. Deng, R. Chen, X. Zhu and Q. Liao, *Chem. Eng. J.*, 2022, **435**, 135025.

11 T. Cheng, R. He, Q. Zhang, X. Zhan and F. Chen, *J. Mater. Chem. A*, 2015, **3**(43), 21637–21646.
12 X. Shao, C. Cao and T. C. Liu, *Remote Sens.*, 2016, **8**(3), 254.
13 L. Ma, J. Wang, F. Zhao, D. Wu, Y. Huang, D. Zhang, Z. Zhang, W. Fu, X. Li and Y. Fan, *Compos. Sci. Technol.*, 2019, **181**, 107696.
14 H. Xie, W. Xu, C. Fang and T. Wu, *Soft Matter*, 2021, **17**(7), 1901–1911.
15 B. Yu, Z. Sun, Y. Liu, Z. Zhang, Y. Wu and F. Zhou, *ACS Appl. Mater. Interfaces*, 2021, **13**(31), 37609–37616.
16 W. Zhao, L. Xiao, X. He, Z. Cui, J. Fang, C. Zhang, X. Li, G. Li, L. Zhong and Y. Zhang, *Opt. Laser Technol.*, 2021, **141**, 107115.
17 J. Wan, J. Xu, S. Zhu, B. Wang, J. Li, G. Ying and K. Chen, *J. Colloid Interface Sci.*, 2023, **629**(B), 581–590.
18 A. Li, Y. Wan, Y. Gao, Z. Tang, J. Xu, M. Huang, Y. Li, X. Zhang and X. Chen, *Mater. Today Nano*, 2022, **20**, 100277.
19 E. Y. Bayar, B. Getiren, F. Soysal, Z. Ciplak, N. Yildiz and E. Bayraktar, *Mater. Res. Bull.*, 2023, **166**, 112352.
20 X. Li, S. Du, C. Ma, T. Shi, W. Qi and H. Yang, *Ceram. Int.*, 2024, **50**(6), 9469–9478.
21 J. Yang, R. Xu, H. Cui, Y. Zhang, X. Chen, J. Zhao and L. Dai, *Prog. Org. Coat.*, 2025, **205**, 109307.